In vivo imaging with a flat, lensless microscope

JESSE K. ADAMS,[†,1,2] DONG YAN,[†,1,2] JIMIN WU,[†,4] VIVEK BOOMINATHAN,[2] SIBO GAO,[2,3] ALEX V. RODRIGUEZ,[2] JENNIFER CARNS,[4] REBECCA RICHARDS-KORTUM,[2,4] CALEB KEMERE,[2,3,4] ASHOK VEERARAGHAVAN,[1,2,5,*] JACOB T. ROBINSON[1,2,3,4,*]

[1]*Applied Physics Program, Rice University, 6100 Main Street, Houston, Texas 77005, USA*
[2]*Department of Electrical and Computer Engineering, Rice University, 6100 Main Street, Houston, Texas 77005, USA*
[3]*Department of Neuroscience, Baylor College of Medicine, One Baylor Plaza, Houston, Texas 77030, USA*
[4]*Department of Bioengineering, Rice University, 6100 Main Street, Houston, Texas 77005, USA*
[5]*Department of Computer Science, Rice University, 6100 Main Street, Houston, Texas 77005, USA*
† these authors contributed equally
*vashok@rice.edu; jtrobinson@rice.edu

Abstract:

Lenless microscopes that form images using simple, compact optics, along with associated computational algorithms provide several advantages: small, inexpensive form factors, large fields of view (FOV), and the ability to refocus an image after capture. To date, however, lensless microscopy has yet to be demonstrated for *in vivo* biological imaging. The primary challenge with *in vivo* bio-imaging is these dense, low-contrast scenes cannot be accurately reconstructed with existing lensless techniques. To overcome this challenge, we designed an optical phase mask that creates a point-spread function consisting of high-contrast contours with a broad spatial frequency spectrum. Here we show that this "contour" phase mask enables *in vivo* imaging where previous lensless imaging technologies have failed. As a proof of concept, we demonstrate 3D imaging of a behaving invertebrate, functional calcium imaging in mouse cortex, and *in vivo* imaging of microvasculature in the human oral mucosa. Together these results demonstrate the ability of lensless imaging to operate in realistic biological imaging applications ranging from pre-clinical animal models to clinical biomedical imaging. Overall, this "Bio-FlatScope" is a clinically relevant imaging technique with advantages of 3D computational refocusing in a low-cost, small form factor that is useful for low-resource settings and difficult-to-reach areas of the body.

Main

Computational imaging algorithms, co-designed with optics and sensors, open up new design degrees of freedom for imaging systems [1–3]. For example, computational imaging techniques have already made a significant impact on microscopy, for applications like super-resolution [4,5], phase imaging [6], and three-dimensional imaging [7,8]. Taken to an extreme, computation can completely replace the traditional lens(es) of an optical system [9], or be combined with light-modulating masks [10,11]. Unlike lens-based imaging systems where the goal is to project a reproduction of a (potentially magnified) scene onto an image sensor, a lensless imaging system seeks to produce an invertible transfer function between the incident light field and the sensor measurements. These measurements often may not resemble a traditional image [12–18] but contain sufficient information for a computational algorithm to reconstruct an image.

45   By removing lenses from the image capture process, systems can achieve substantial
46   improvements in the FOV, preform three-dimensional capture and refocusing, capture light
47   with high-efficiency, and be miniaturized into small form factors [10–12,19].

48   Despite the transformative potential of lensless microscopy, there are currently no
49   demonstrations of *in vivo* biological imaging due to the fact that biological scenes are dense,
50   dim, and low contrast, which can often result in noisy reconstructed images. Indeed, previous
51   lensless microscopy demonstrations have relied on sparse, bright, or high-contrast samples
52   where strong regularization and/or deblurring can be used to reconstruct estimates of the
53   original image [10,19,20].

54   To address the challenge of biological imaging we designed a phase mask especially suited
55   for the low-contrast challenges expected in biological imaging. The key feature of this phase
56   mask is that it achieves a high-contrast and spatially localized sparse point spread function
57   (PSF) that captures textural frequencies common in natural and biological samples (Fig 1d). To
58   create this PSF we generate Perlin noise and apply uncanny edge detection [3]. Figure 1b shows
59   the simulated modulation transfer function (MTF) of our contour-based PSF compared to other
60   PSFs used in lensless imaging systems. The relatively flat MTF spectrum indicates that
61   information from most spatial frequencies are well-preserved by the optical transfer function
62   leading to improved image reconstruction for dense, low contrast samples like biological tissue.
63   We chose to create this PSF using a phase mask (Fig. S2), because phase masks are capable of
64   producing a wide variety of PSFs [21–26] and allow higher light throughput compared to
65   amplitude masks (which block some of the incoming light) [10]. We refer to this prototype
66   device (Fig 1a) as a "Bio-FlatScope" because it achieves a similar flat form factor as previously
67   reported "FlatScopes" [10], but the new contour phase mask allows us to perform the first
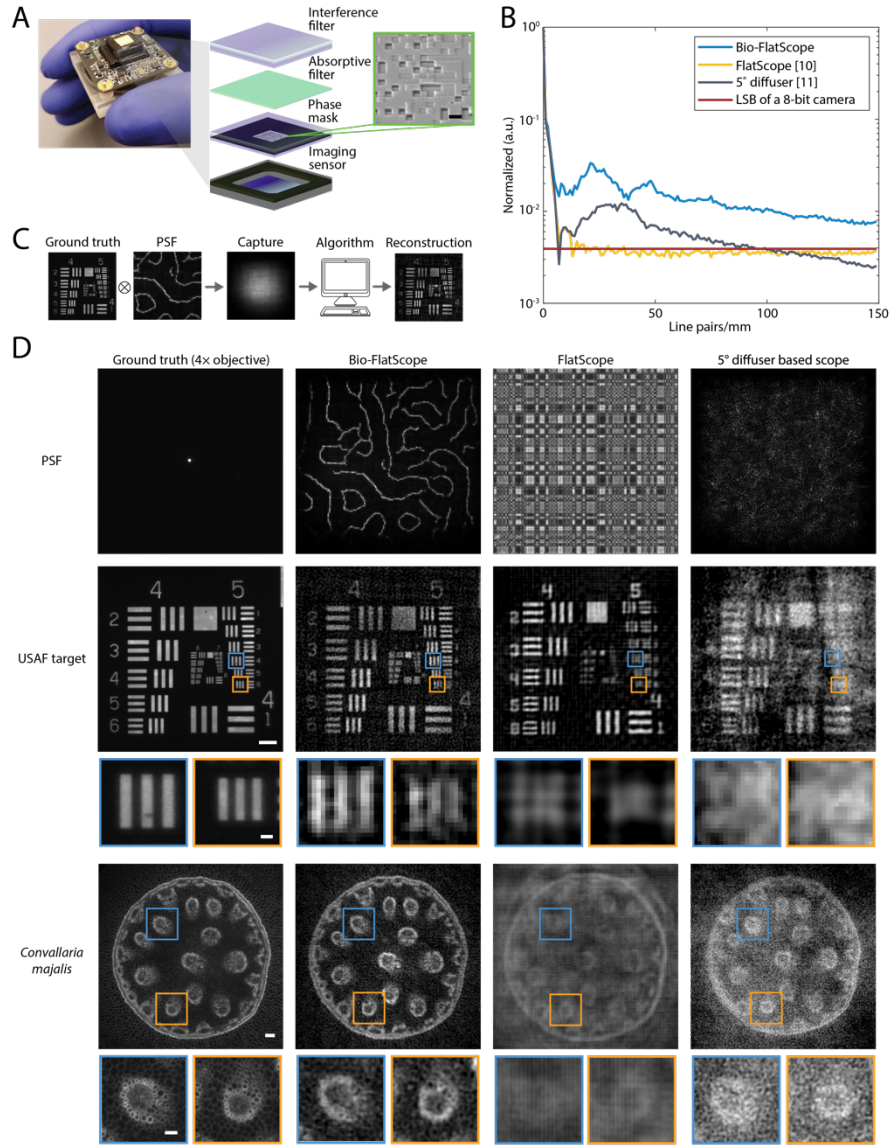68   accurate lensless imaging of biological tissue *in vivo*.

Fig. 1. Bio-FlatScope for *in vivo* fluorescence imaging. (A) Photo of a Bio-FlatScope prototype including the off-the-shelf board level camera. Zoom-in shows components that filter excitation light and apply the phase mask transfer function to the incident light. Also shown is a scanned electron micrograph of a portion of the fabricated phase mask. Scale bar 4 μm. (B) Modulation transfer function (MTF) comparison among PSF designs used by lensless imaging systems show that the contour PSF used for the Bio-FlatScope contains more high-frequency components, which contributes to improved performance. LSB: least significant bit. (C) Flow chart showing the imaging procedure of Bio-FlatScope. (D) High spatial resolution images of a USAF test target and fixed biological samples. Row 1: PSF captures of different lensless imaging systems. Row 2: Ground truth captured by an epifluorescence microscope and reconstructed by 3 different lensless imaging systems. While FlatScope and Bio-FlatScope both show good performance for the high-contrast USAF target, only the Bio-FlatScope performs well on the low-contrast, dense *Convallaria* sample. USAF 1951 Resolution test target scale bar, 100 μm. Insets below show zoom-ins of group 5, elements of 4 & 6. Scale bar, 10 μm. Convallaria majalis scale bar, 100 μm. Insets below show zoom-in comparisons. Scale bar, 50 μm.

Results

To evaluate the performance of Bio-FlatScope, we constructed prototypes using Sony IMX178 monochromatic 6 MP imaging sensors with 2.4 μm pixels. Phase masks were fabricated using a two-photon lithography system (Nanoscribe, Photonic Professional GT2) for ease of prototyping (see *Methods*). The contour-based phase masks were designed with a minimum feature width of 6-12 μm.

Spatial Resolution & Fixed Biological Samples

Using USAF resolution targets, we found that reconstructed images taken by the Bio-FlatScope achieve < 9 μm lateral resolution. We measured this resolution by capturing images of a negative 1951 USAF Resolution Target (Edmund Optics #59-204) with an added fluorescent background. Multiple images were captured at 15 ms each and averaged to remove noise. Excitation light was provided in a near-epi configuration with a fiber/microprism (Fig S3). Images were captured at a distance of ~4 mm. In Fig. 1d, we show that we can achieve < 9 μm resolution. While this spatial resolution is reduced by ~1.5× - 3.5× compared to (single-photon) miniature microscopes (see Table S1), we find that our system achieves cellular resolution under sparse labeling conditions.

The main advantage of the Bio-FlatScope is its ability to accurately reconstruct dense, dim, and low-contrast biological samples; thus, we compare the performance of Bio-FlatScope to other lensless imaging techniques for imaging a fluorescent biological sample. Specifically, we compared reconstructed images of *Convallaria majalis* (lily of the valley) stained with green fluorescent protein (GFP). We notice that for the high-contrast USAF test targets, both the FlatScope and Bio-FlatScope show clear image reconstructions; however, for the *Convallaria*, only the Bio-FlatScope shows good correspondence to ground truth images captured with a 4× microscope objective (Nikon Fluor) (Fig. 1d). These data are based on multiple images of the *Convallaria* slice (at ~3.5 mm from the device) captured at 200ms each in the near-epi configuration and averaged for noise removal. Note in the *Convallaria* insets that for the lensless approaches tested, only the Bio-FlatScope can resolve some of the large circular plant cells with sizes of around 10 μm. We also confirmed that Bio-FlatScope can resolve images in fixed neural tissue using *ex vivo* mouse brain slices (deep cortex and hippocampus) expressing the fluorescent protein GCaMP6f (see *Methods*). Here we capture 20 images at a distance of ~5.3 mm using transmissive illumination with 1s exposures averaged to remove noise. Comparisons between Bio-FlatScope images and ground truth microscopy show clear delineation between cortex layer 2/3, corpus callosum and hippocampus (CA1) (Fig. S4). We can also identify clusters of neurons in the cortex as well as the pyramidal layer of CA1 (see far-right column of Fig. S4).

Single capture three-dimensional imaging in vivo

One significant advantage for lensless imaging is the ability to obtain three-dimensional information with a single image capture due to the fact that the PSFs change as a function of depth. To demonstrate that Bio-FlatScope is also capable of single-shot 3D reconstruction of biological samples we imaged *Hydra vulgaris*, a freshwater cnidarian polyp, which has a simple, yet dynamic network of neurons, optical transparency, and the ability to regenerate from a small patch of tissue [27,28]. An additional advantage of *Hydra* is their genetic tractability and a number of transgenic lines including lines that express GFP or calcium dependent fluorescent protein GCaMP7b [29], as well as their compatibility with microfluidic devices [27]. Using Bio-FlatScope we captured videos at 1 Hz of *Hydra* expressing GFP in interstitial cell lineage. We were then able to reconstruct these images in three dimensions (Fig. 2a) during post-processing using
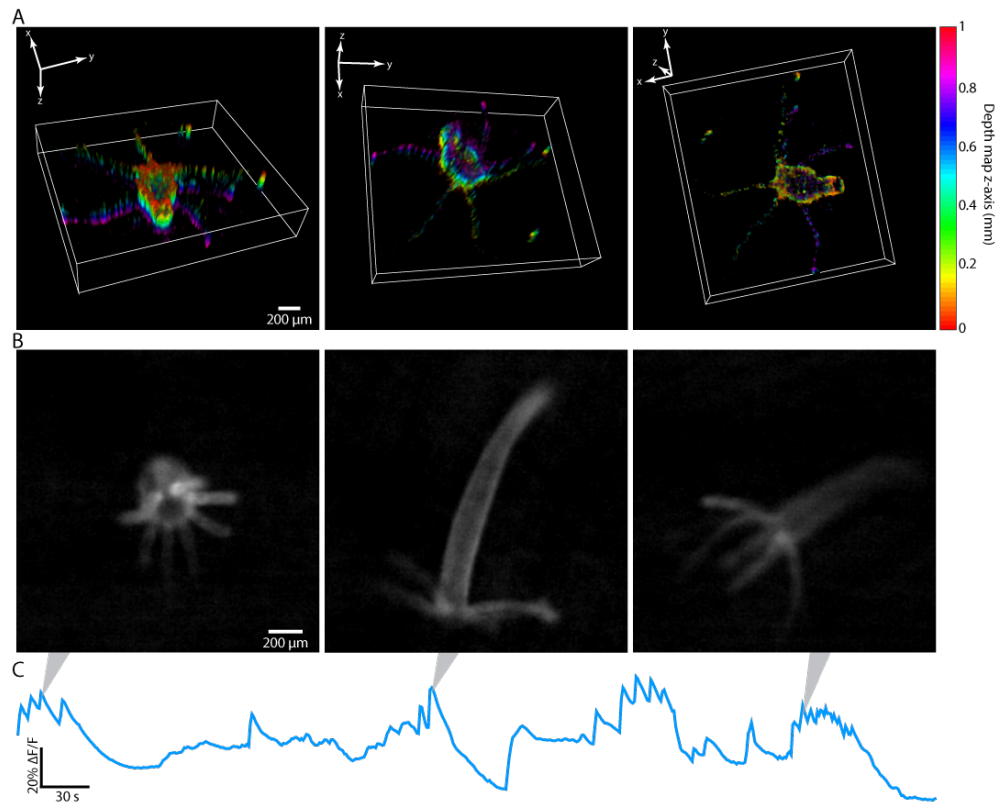
Fig. 2. Ca²⁺ imaging (GCaMP7b) and three-dimensional imaging (GFP) of *Hydra vulgaris in vivo*. (A) Select angles of three-dimensional Bio-FlatScope reconstructions of *Hydra vulgaris* expressing GFP in the interstitial cell lineage. Colors represent relative depth location along the z-axis. Scale bar, 200 μm. (B) Selected Bio-FlatScope reconstructed frames of video of *Hydra vulgaris* expressing GCaMP7b in muscle cells. Scale bar, 200 μm. (C) ΔF/F traces showing the Ca²⁺ responses over a 5-minute recording.

117   a series of PSFs corresponding to different distances from the sensor in 50 μm increments. Here
118   we show a 4 mm³ volume reconstructed from a single capture. By contrast traditional
119   microscopes typically require scanning spatially, axially, or both. This single-capture, three-
120   dimensional imaging opens up the possibility for high-resolution, high-speed, volumetric
121   imaging of whole organisms freely behaving over large FOVs.

122   *In vivo epifluorescence calcium imaging of whole animal with Hydra vulgaris*

123   Given the high-speed volumetric imaging made possible by single-shot 3D imaging, we tested
124   the ability of Bio-FlatScope to capture whole-animal dynamic calcium activity in *Hydra*. We
125   began by imaging *Hydra vulgaris* expressing GCaMP7b in muscle cells [30]. We captured
126   video of *Hydra* freely behaving at 2 Hz over a FOV > 12 mm². In Fig. 2b&c we show selected
127   frames from a video of the reconstruction as well as the overall change in fluorescence over
128   time (ΔF/F). The recordings show strong calcium responses during contraction events as
129   reported previously [31] (full video shown in Visualization 1). Although movement of the
130   animal can produce some noise in the ΔF/F signal, the deformable Hydra body makes it difficult
131   to generate adaptive ROIs that move with the animal. Nevertheless, the bright synchronous
132   calcium activity in the Hydra peduncle allows for fixed ROIs to effectively capture calcium
133   dynamics [27,32]. Here the large FOV and 3D reconstructions help us capture movies of whole-
134   animal calcium dynamics, which can be used by neuroscientists to study information processing
135   in these small model organisms [33].

136 *In vivo epifluorescence calcium imaging in mice*

137 We also found that the Bio-FlatScope is capable of imaging calcium dynamics in mouse cortex,
138 which is commonly used for neuroscience experiments and preclinical testing [34-37]. This
139 type of *in vivo* imaging is particularly difficult for lensless imaging and epifluorescence
140 imaging because tissue scattering causes blurring and loss of contrast.

141 We hypothesized that the optimized contour PSF with high contrast features will provide
142 good protection against noise amplification in these low-contrast scenes and allow Bio-
143 FlatScope to perform reconstructions through scattering media similar to epifluorescence
144 imaging (Fig. S5).

145 To test our hypothesis, mice expressing GCaMP6f in the motor cortex (see *Methods*) were
146 head-fixed and placed upon a freely moving treadmill to allow for locomotion during video
147 capture (Fig. 3a). We recorded calcium imaging movies over a FOV of ~ 16 mm^2 of the entire
148 cranial window (Fig. S6) using a 473 nm excitation light source (see *Methods*). A cropped
149 region near the injection site is shown in Figure 3c. Compared to previously reported miniature
150 microscopes with cellular resolution [38], we achieve more than a 30× increase in the FOV (see
151 Table S1). We also measured the velocity of the treadmill during imaging sessions and
152 synchronized the image captures with this velocity data. During the recording sessions, we
153 applied a brushing tactile stimulation in 30 s intervals to encourage locomotion and neural
154 response in the motor cortex. Correlation between locomotion (as performed by the mouse here
155 on a treadmill) and neuronal response in the motor cortex has been established in prior
156 reports [39–41] and is confirmed in our epifluorescence imaging. In the regions of high activity
157 in the motor cortex, we observed peak fluorescence signals during locomotion an average of
158 $\sim 3 \times$ greater than periods of no motion (rms) and were able to resolve blood vessels as small as
159 ~ 10 μm in diameter. To compare our Bio-FlatScope imaging to conventional epifluorescence,
160 we replaced the Bio-FlatScope with a 4× objective lens and fluorescence microscope. We
161 performed epifluorescence imaging under the same conditions within 30 minutes of our Bio-
162 FlatScope recordings (see *Methods*) and found very similar spatiotemporal dynamics in the two
163 data sets (Fig. 3, Fig. S7 and S8). We chose the 4× objective lens to accommodate the FOV
164 captured by Bio-FlatScope (while maintaining high resolution) and registered both data sets to
165 accommodate for movement [42,43].

166 To compare Bio-FlatScope data with epifluorescence data, we selected 4-second windows
167 time-aligned to the response to stimulation (reflected as a large change in ambulatory activity
168 of the mouse) over a two-minute period (Fig. 3d&e, shown in green). Ambulatory activity was
169 determined by synchronizing the wheel velocity with the imaging data for both Bio-FlatScope
170 and epifluorescence (shown in Fig. 3d&e for a single ROI, Visualization 2 shows video for
171 multiple regions). We validated the similarity of the windowed ΔF/F responses with correlation,
172 finding a median correlation coefficient of 0.852 with interquartile range (IQR) of 0.131 (Fig
173 3f, left-side). We also compared data from time windows of little to no locomotion, where
174 velocity < 1 cm/s (windows shown in Fig. S7) with epifluorescence captured motion resulting
175 in a median correlation coefficient of -0.375 and an IQR of 0.513 (Fig 3f, right-side). As
176 expected, data from regions of motion/stimuli highly correlate when comparing Bio-FlatScope
177 to epifluorescence data (coefficients range from 0.65 to 0.97, $p < 0.001$), while regions of little
178 to no motion show more random correlation (coefficients ranging from -0.52 to 0.31, two values
179 of $p < 0.001$ and six values of $p > 0.05$), confirming that using Bio-FlatScope we can capture
180 behaviorally relevant calcium dynamics that are comparable to traditional dynamics capture
181 with conventional epifluorescence microscopes.

182 In addition, when plotting the time of the calcium peaks over the FOV we find that when
183 the animal initiates movement the majority of early peaks appear in the bottom and right of the
184 FOV and the majority of late peaks appear in the top and left (Fig. 3g). This pattern is also
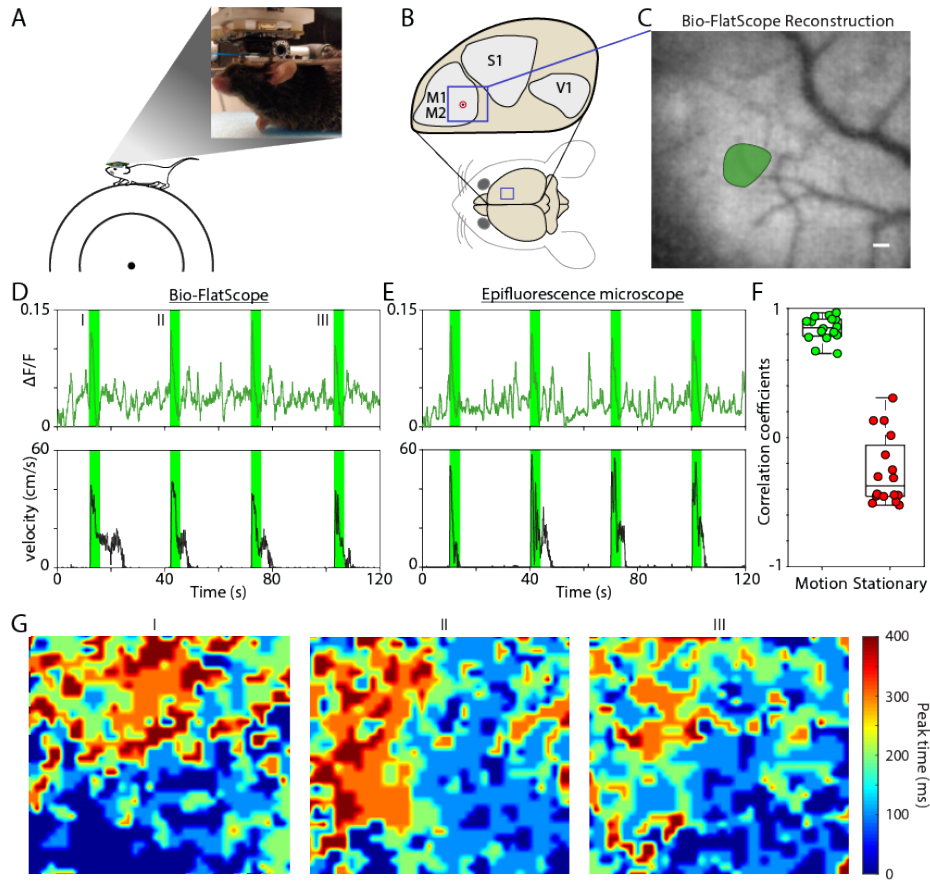
Fig. 3. Comparison of Bio-FlatScope to epifluorescence during stimulus-evoked Ca^{2+} responses in motor cortex. (A) Experimental setup for Bio-FlatScope for imaging a head-fixed mouse on a freely moving treadmill. Zoom-in shows a photo of a mouse on the treadmill with Bio-FlatScope in place (B) Target region in the mouse brain. The blue square region indicates the approximate location of the cropped FOV (in the motor cortex). The circle with the black dot indicates the approximate region of injection for GCaMP6f. (C) Bio-FlatScope reconstruction with a single ROI of high-activity marked. Scale bar, 100 μm. (D) ΔF/F trace and treadmill velocity for Bio-FlatScope during recording session. The rising edge of the 4-second windows in green correspond to the application of tactile stimuli. (E) ΔF/F trace and treadmill velocity for epifluorescence during recording session. (F) Box plot showing correlation coefficients comparing stimulus-evoked Ca^{2+} responses from Bio-FlatScope to epifluorescence (shown in green), and comparison of periods of little or no motion with Bio-FlatScope to stimulus-evoked Ca^{2+} responses with epifluorescence (shown in red) for the ROI. (G) Heat maps for Bio-FlatScope reconstructions showing spatiotemporal Ca^{2+} dynamics time-aligned with stimuli (at I, II, and III). Colormap shows the time at which pixels have their peak response for ΔF/F during a 400 ms period. These data show that when initiating movement, neural activity consistently begins in the lower right and propagates to the upper left.

185 observed with epifluorescence imaging confirming that Bio-FlatScope measures similar
186 spatiotemporal Ca^{2+} dynamics (images are processed for visualization, see Fig. S8 for
187 epifluorescence data). The recorded video was captured at 10 Hz (50 ms exposures) and shows
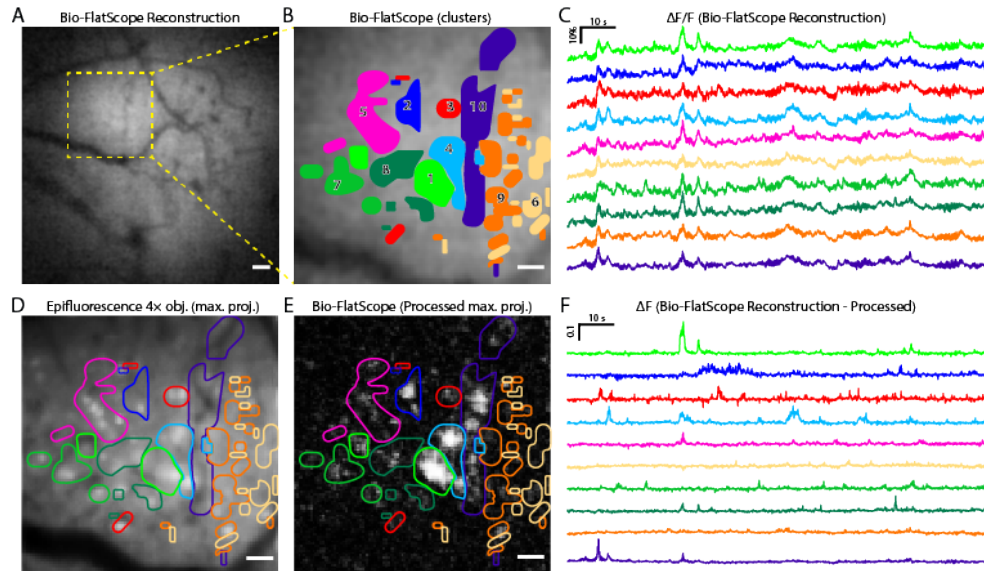188 a period of 400 ms following the tactile stimulation.

Fig. 4. Extracting near cellular-sized Ca^{2+} signals from Bio-FlatScope reconstructions. (A) Cropped region of Bio-FlatScope reconstruction of a single frame with a high-activity region shown by a dashed box. Scale bar, 100 μm. (B), Zoom-in on the region of high-activity with overlay of clusters determined through post-processing using RPCA and k-means. Scale bar, 50 μm. (C) ΔF/F traces from Bio-FlatScope reconstruction video over during two-minute recording corresponding to the clusters. (D) Maximum projection from epifluorescence recording of same high activity region with overlay of clusters determined from Bio-FlatScope data. Scale bar 50 μm. (E) Maximum intensity projection of Bio-FlatScope reconstruction data processed using RPCA with overlay of clusters. Scale bar 50 μm. (F) ΔF traces from Bio-FlatScope reconstructions after post-processing using RPCA.

189

190   We can also extract unique calcium activity from small regions of interest (ROIs) that
191 approach the size of individual cells. To capture this data, we rely on the fact in the time domain,
192 some Ca^{2+} activity in individual or small groups of cells appear as outliers compared to the
193 background activity. Robust Principal Component Analysis (RPCA) excels at determining such
194 sparse outliers [44,45], and so we used the RPCA algorithm to identify these regions of high
195 calcium activity. We then used K-means to identify which high-activity regions show correlated
196 activity. These clustered ROIs represent distinct calcium signals from areas that are the size of
197 a few individual cells. When we compared the ROIs determined through RPCA and k-means
198 from Bio-FlatScope we found close correspondence to bright individual neurons observed from
199 epifluorescence microscopy (Fig. 4d). Additionally, the calcium activity in each of these ROIs
200 show unique temporal dynamics suggesting that calcium dynamics might be recovered with
201 near cellular resolution.

202   It is important to note that the blurring and loss of contrast resulting from scattering affects
203 the properties of the scene but has no direct effect on the performance of our reconstruction
204 algorithm because the reconstruction algorithm makes no assumptions about the medium
205 between the source and the imager. Compared to epifluorescence microscopy, the only
206 additional effect of scattering on lensless imaging is the fact that noise is amplified by the
207 reconstruction algorithm, which is true for all lensless imaging reconstruction techniques, and
208 mitigated by the contour PSF of Bio-FlatScope.

209 *Human oral mucosa imaging*

210 In addition to pre-clinical imaging, we found that the Bio-FlatScope can image human
211 microvasculature *in vivo*, which is a clinically relevant biomarker for diseases like sepsis [46,
212 47], oral neoplasia [48-50], and esophageal neoplasia [51-54]. To test our ability to image
213 microvasculature we imaged oral mucosa in healthy human volunteers. The Bio-FlatScope
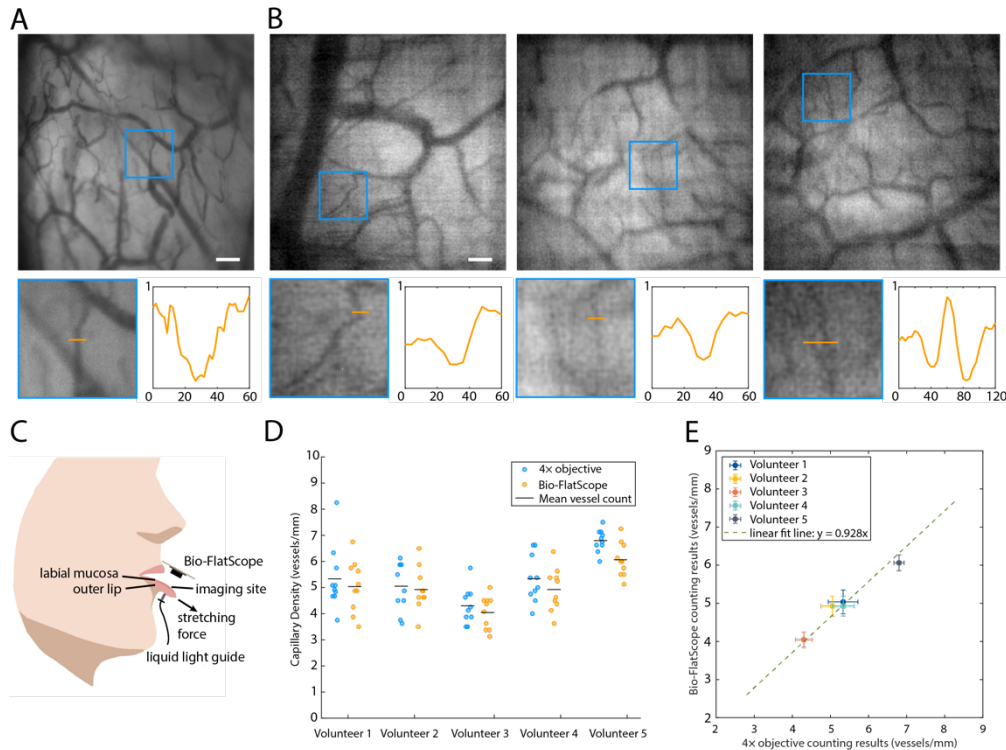
Fig. 5. Human oral mucosa imaging. (A) Images acquired using a 4× objective. Scale bar, 200 μm. (B) Reconstructed images from a Bio-FlatScope prototype. Each blue square indicates a sub-region which contains ~15 μm diameter vessels. Scale bar, 200 μm. Left insets, zoom-ins of sub-regions. Right insets, pixel intensity along the cross section (shown as orange bars) of the vessels. Length of orange bars in insets, 60 μm (120 μm in the 4th inset). X-axis: distance (in μm) from the left origin of the orange bar. Y-axis: Pixel intensity in normalized arbitrary units, shared by all 4 plots. (C) Experimental setup. The transmissive illumination is delivered by a liquid light guide connected to a green LED light source. (D) Vessel counting results of each volunteer. Each outlined circle corresponds to a different region on the lip. Less translucency indicates overlapping dots. There are 10 circles in each column. (E) Relationship between 4× objective and Bio-FlatScope counting results. Each circle is the average of 10 different lip regions as shown in panel D. Note that we imaged the same approximate of the labial mucosa with both the 4X and Bio-FlatScope; however, were unable to capture images of the exact same area of tissue when switching between imaging modalities. The error bars show the standard error of the mean.

prototype was placed a few millimeters away from the inner surface of the lower lip to image the microvasculature in the labial mucosa using transillumination with a green LED coupled to a liquid light guide in contact with the outer surface of the lower lip (Fig. 5). We can see in Fig. 5a&b that Bio-FlatScope successfully reconstructed the morphological characteristics of microvasculature in labial mucosa with contrast comparable to a 4× objective, and with the ability to resolve micro vessels less than 20 μm in diameter. The measurements in Fig 5d&e were based on images captured from 10 different nearby regions. Importantly we find that individual differences in microvascular density measured with a 4× objective lens correlate with those measured using the Bio-FlatScope. For this comparison we captured 4× and Bio-FlatScope images from approximately the same region of the oral mucosa; however, because there was no way to accurately register images between recording modalities, all measurements represent slightly different regions of tissue. Changes in microvessel density are important in a number of clinical scenarios: angiogenesis is a hallmark of cancer [55]; microvessel density is correlated with prognosis for a number of cancers [56, 57]; and sub 20-μm vessel density has been proposed as a biomarker of sepsis [46,47].

229   The ability to quantify microvascular density combined with the ability to measure vessel
230 morphology suggests that our lensless imaging technology could be used for clinical
231 microvascular imaging with key advantages associated with lensless imaging. Specifically, our
232 small form factor is useful for accessing difficult-to-reach areas of the body and is advantageous
233 for low-resource settings where high resolution in vivo imaging techniques may be
234 prohibitively expensive. This approach enables more patient-friendly form factors and larger
235 fields of view compared to conventional microscopes. In addition, Bio-FlatScope has
236 advantages compared to conventional microscopy where the ability to capture 3D information
237 and to computationally refocus could enable rapid imaging over curved surfaces and provide
238 additional diagnostic information.
239

Discussion

241 Here we have demonstrated structural and functional imaging of biological samples using
242 lensless microscopes with cellular resolution (~9 micron), large FOVs >16 mm^2, digital
243 refocusing, and single capture, three-dimensional imaging over volumes of 4 mm^3. The key
244 innovation of a contour PSF enables what is, to the best of our knowledge, the first *in vivo* Ca^{2+}
245 imaging and human microvascular imaging with a lensless microscope.
246   Key next steps will be to improve the packaging and electronic components to make
247 compact devices that could be used for preclinical studies of dynamic calcium activity,
248 endoscopy and superficial biomedical imaging. In the case of Ca^{2+} imaging we were able to
249 extract localized Ca^{2+} signals ranging in area from 150 μm^2 to 0.01 mm^2 using RPCA. These
250 results serve as a proof-of-principle that lensless microscopy provides a route toward high-
251 resolution and large FOV calcium imaging in a small lightweight form factor. By reducing (or
252 rearranging) the electronic components around the imaging sensor, we foresee miniaturizing
253 our device to the point that we can mount it atop a mouse or small animal to study calcium
254 activity during unrestricted behavior, similar to mini-scopes, but with a superior combination
255 of spatial resolution and field of view.
256   While the resolution shown here appears to meet the needs for microvascular imaging and
257 approaches cellular resolution Ca^{2+} imaging, there is still room for improvement. This
258 improvement could be realized by optimizing the masks for closer scene-to-mask distances.
259 These closer distances will not only improve spatial and axial resolution but will increase light
260 collection efficiency and reduce the form-factor enabling easier integration. Additionally,
261 integration of the device can allow for a smaller refractive index change between the sample
262 and device surface, which can cause a slight barrel effect at the edge of the FOV. As one brings
263 the device closer to the sample, there is a corresponding decrease in the FOV until it matches
264 the size of the sensor. To increase the effective FOV, future devices could be arrayed to
265 maintain large scene coverage while maintaining a thin device profile.
266   Other modifications to the design could further improve performance. Integration of the
267 excitation light source (or multiple sources) can be introduced to improve the illumination
268 coverage over the FOV. For this purpose, commercially available micro-LEDs or integrated
269 waveguides can be used at little to no cost to form factor. To improve on the low-light
270 capabilities necessary for quality fluorescence microscopy, sCMOS imaging sensors or single
271 photon avalanche diodes (SPADs) could be integrated to increase the SNR which is so
272 important in lensless imaging. In addition to physical alterations of the lensless system,
273 integration of new computational methods for imaging through scattering media might be used
274 to extract additional three-dimensional information for brain imaging. One important
275 opportunity for this class of lensless *in vivo* imagers is the potential to image tens of thousands
276 of neurons simultaneously in a freely moving animal. Additionally, because our system is
277 designed to capture incoherent sources, other imaging modalities like brightfield, darkfield and
278 reflected-light microscopy are also possible, as we demonstrated in the case of microvascular

279 imaging without the use of any contrast agents. These lensless microscopy modalities could be
280 useful for endoscopy and point-of-care diagnostics.
281   Overall, technologies based on Bio-FlatScope can be applied to a number of challenging
282 microscopy problems where high temporal resolution, large FOV, and small form-factor are
283 outside the capabilities of traditional lens-based microscopy.
284
285 **Methods**

286 *Calibration*

287 The PSF of the mask must be learned prior to capturing scenes through a one-time calibration
288 process. Because we cannot capture images of an ideal point source, we instead use a single
289 10µm fluorescent microsphere (FluoSpheres yellow-green), which is closely aligned to the
290 center of our mask. The fluorescent bead was dropcast onto a microscope slide, then protected
291 by a coverslip (Nexterion, 170 µm thick). Images of the PSF were captured for each depth (i.e.,
292 distance axially from the device) of interest by Bio-FlatScope with the bead located
293 approximately at the center of the phase mask. Calibration images were averaged through
294 multiple captures and background was subtracted to ensure the highest SNR for the PSFs. The
295 sensitivity of the system to depth requires calibration images of PSFs to be taken over a range
296 of distances, which allow for refocusing and three-dimensional reconstruction in post-
297 processing.

298 *Reconstruction*

299 To reconstruct images, we effectively solve the following minimization problem, adding
300 Tikhonov regularization to the deconvolution to avoid noise amplification:

$$\hat{\mathbf{i}} = \arg\min_{\mathbf{i}} \|\mathbf{b} - p * \mathbf{i}\|_F^2 + \frac{\gamma}{2}\|\mathbf{i}\|_2^2$$

301

302 where $*$ denotes convolution, $\hat{\imath}$ is the estimate of the scene, $\mathbf{i}$ is the scene, $\mathbf{b}$ is the sensor
303 measurement, p is the PSF at the scene distance, γ is the regularization weight, and F is the
304 Frobenius norm. This minimization problem can be solved by closed form via Wiener
305 deconvolution as:

$$\hat{\mathbf{i}} = \mathcal{F}^{-1}\left(\frac{\mathcal{F}(p)^* \odot \mathcal{F}(\mathbf{b})}{|\mathcal{F}(p)|^2 + \gamma}\right)$$

306

307 where $\odot$ denotes Hadamard product, F denotes a Fourier transform and F^{-1} denotes an inverse
308 Fourier transform. To reconstruct three-dimensionally, we solve the same minimization
309 problem, but do so for the sum of distances of interest:

$$\hat{\mathbf{i}}_D = \arg\min_{\mathbf{i}_D} \|\mathbf{b} - \sum_{d=1}^{D} p_d * \mathbf{i}_d\|_2^2 + \frac{\gamma}{2}\|\mathbf{i}_D\|_1$$

310

311 where D is the number of distances, d, from the imaging device.

312 *Excitation Light*

313 Excitation light for Bio-FlatScope was achieved both transmissively and in near-epi
314 configurations. Transmissive illumination was provided either using light through an epi-
315 fluorescent microscope objective (Nikon Fluor 4×, NA 0.13 PhL DL), or using a near-
316 collimated 470 nm LED (Thorlabs, M470L3) with an incorporated GFP excitation filter
317 (Thorlabs, MF469-35). Near-epi illumination was provided using a fiber-coupled 475 nm LED
318 (Prizmatix, UHP-T-475-SR) with an incorporated GFP excitation filter (Thorlabs, MF469-35).
319 The light was coupled into a multimode fiberoptic cable (Thorlabs M72L01 200 µm diameter
320 core, NA 0.39 or Edmund Optics, #57-749 400 µm diameter core NA 0.22) with an aluminum
321 coated microprism (Edmund Optics 0.18 mm #66-768 or 0.70 mm #66-773) adhered to the

322 exposed tip of the fiber with optical epoxy (Norland, NOA72). The microprism was placed near
323 the surface of the lensless imaging device.

Fabrication

325 Bio-FlatScope prototypes were constructed using an off-the-shelf board level camera (Imaging
326 Source, DMM 37UX178-ML) with a monochrome Sony CMOS imaging sensor (IMX178LLJ,
327 6.3 MP, 2.4 μm pixels). The phase mask was fabricated using a 3-D photolithographic system
328 (Nanoscribe, Photonic Professional GT2) using a photoresist (Nanoscribe, IP-L 780) on a 700
329 μm SiO2 substrate. The substrate was then cut down to more closely match the sensor size of
330 the camera (and filters). The substrate was masked with an opaque material to provide an
331 aperture containing only the phase elements. The substrate with phase mask was affixed atop
332 the imaging sensor, followed by a hybrid filter, similar to Richard et al. [58], but using a
333 commercially available absorptive filter (Kodak, Wratten #12) placed below an interference
334 filter (Chroma, ET525/50m), both cut to the sensor size requirements (see Fig. 1a). A housing
335 was 3D printed (MJP 2500) to hold the phase mask and filters atop the imaging sensor.

Mouse Brain Slice

337 All experiments were approved by the Rice University IACUC. Mice were sacrificed 14 days
338 post-injection of AAV9-CamKII-GCaMP6f in the CA1 region of the hippocampus. From
339 bregma, the injection site was +2 mm medial/lateral, -2 mm anterior/posterior and -1.65 mm
340 deep. The total injection amount was 0.5 μL at a rate of 0.05 μL/min. The brain expressing
341 GCaMP6f was cryoprotected in 30% sucrose, embedded in OCT compound (Tissue-Tek),
342 frozen and sliced into 50 μm slices using a cryostat (Leica). Slices were then rinsed in 1x
343 phosphate-buffered saline (PBS) and mounted using Vectashield H-1000 with DAPI (Vector
344 Labs) then sealed with coverslips.

Hydra vulgaris

346 *Hydra* were cultured in *Hydra* media using the protocol adapted from Steele Lab (UC Irvine)
347 at 18°C with 12:12 hours light-dark cycle. Animals were fed freshly hatched artemia every 2
348 days and cleaned after 4 hours. Transgenic lines developed by embryo microinjections [28]
349 expressing either GFP in interstitial cell lineage (GFP, Neurons) or GCaMP7b in endodermal
350 muscle cells (GCaMP7b, Endo) were used. The transgenic line of Hydra expressing GFP under
351 actin promoter was originally developed by Steele Lab and selected for expression in neurons.
352 The transgenic line of *Hydra* expressing GCaMP7b under EF1a promoter was developed by
353 Robinson Lab and Juliano lab (UC Davis) selected for expression in endodermal muscle cells.
354 Both *Hydra* expressing GFP and GCaMP7b were imaged in hydra media on petri dishes
355 with coverslip bottoms (MatTek, 35 mm, 14 mm #1.5, coverslip). Bio-FlatScope images were
356 captured through the coverslip with excitation light provided by the fiberoptic cable/microprism
357 combination.

Brain tissue phantom

359 The brain tissue phantom was created by suspending non-fluorescent polystyrene
360 microspheres (Polybead Acrylate Microspheres, 1 μm diameter, 4.55×10^{10} beads/mL) in
361 polydimethylsiloxane (PDMS) (Sylgard, Dow Corning; 10:1 elastomer:cross-linker weight
362 ratio). For the brain tissue phantom, a concentration of 5.46×10^9 beads/mL was used to achieve
363 a scattering coefficient of ~1 mm^{-1} to simulate the reported scattering coefficients in mouse
364 brain tissue [60,61]. Microspheres (0.6 mL) were added to isopropyl alcohol (0.6 mL) and
365 vortexed thoroughly for uniformity. The microsphere/alcohol mixture was added to 4 g of the
366 PDMS elastomer and mixed thoroughly, followed by 0.4 g of crosslinker and again mixed
367 thoroughly for uniformity. The desired thickness of 140 μm was achieved by spin-coating the
368 mixture onto a SiO2 wafer. then heated at 37ºC for 30 minutes.

Illumination strategy for fluorescence imaging

For fluorescence imaging we illuminated the sample with a fiberoptic cable attached to an aluminum-coated microprism [61]. This illumination strategy is capable of fitting into the small space between the lensless imager and biological sample. To prevent the excitation light from reaching the sensor and overwhelming the fluorescence signal we constructed a hybrid excitation filter that combines an absorptive and interference filter [58] and attached it to the top of the phase mask. The thickness between the image sensor and surface of device is ~5 mm.

Animals for in vivo mouse brain imaging

Wild-type C57BL/6 mice (n=3) from Charles River Laboratories were used for this study. Animals are housed with standard 12 h light/dark cycle with ad libitum food and water. All animals (n=3) were injected with the adeno-associated viral vector AAV9.CamKII.GCaMP6f.WPRE.SV40 (Penn Vector Core). All experimental procedures were approved by the Institutional Animal Care and Use Committee at Rice University and followed the guidelines of the National Institute of Health.

Headpost Implant and Cranial Window Design

Headpost implant design was adapted from Ghanbari et al. [62], and consists of a custom-made Titanium or Stainless-steel head-plate, a 3D-printed frame, and three 0-80 screws to hold the frame to the head-plate. We fabricated the head-plate with Titanium or Stainless-steel plate (McMaster-Carr) using a waterjet system (OMax), and 3D printed the frame using a ProJet MJP 2500 (3D Systems). Our design files can be found online (https://github.com/ckemere/TreadmillTracker/tree/master/UMinnHeadposts). We assembled the headpost implant after tapping the 3D printed frame with 0-80 tap and securing the head-plate over the frame with three screws. The entire headpost is then stored in 70% Ethanol prior to surgery.

Cranial window fabrication procedure was adapted from Goldey et al. [63]. Windows were made of 2 stacked round coverslips (Warner Instruments # CS-3R, CS-4R, CS-5R) of different diameters. To fabricate the stacked windows, a 3 mm (or 4 mm) round coverslip was epoxied to a 4 mm (or 5 mm) cover slip using an optical adhesive (Norland Products Inc. e.g. # NOA 61, 71, 84) and cured using long-wavelength UV light. To accommodate the large 5 mm stacked window, we cut off the right side of the 3D-printed frame to allow for extra space for the C&B Metabond to bind to the skull outside of the stacked cranial window. Fabricated stacked windows were stored in 70% ethanol prior to surgery.

Surgical Procedures

For AAV9 injections, mice were anesthetized with 1-2% isoflurane gas in oxygen and administered sustained release Buprenorphine SR-LAB (Zoofarm, 0.5 mg/kg). A small craniotomy was carefully drilled at the target location. A total of 0.5-1 μL of AAV9 virus was injected slowly at a rate of 0.07 μL/min into each mouse with a Hamilton syringe paired with syringe pump controller (KD Scientific # 78-0311). Specifically, mouse W1 was injected at -1.5 AP; +1.5 ML; -0.25 DV targeting the motor cortex; mouse W2 was injected at -1.67 AP; +1.1 ML; -0.25 DV targeting the motor cortex; mouse W3 was injected at -1.23 AP; +1.23 ML; -0.25 DV targeting the motor cortex. Following the injection, a small amount of bone wax was applied over the craniotomy, while taking care not to press down on the brain surface. The incisions were closed using a small drop of Vetbond (3M), and the mice were allowed to express for at least 4 weeks before headpost and window implantation.

For headpost and window implantation, mice were administered Buprenorphine SR-LAB (0.5 mg/kg) and Dexamethasone (2 mg/kg) 30 min prior to the craniotomy procedure. Mice were anesthetized with 1-2.5% of isoflurane gas in oxygen and secured on a stereotax (Kopf Instruments) using ear bars. A single large cut was made to cut away the majority of the skin

above the skull while attempting to match the 3D printed frame to the exposed skull. We then used a 3 mm (or 4 mm, depending on the window implant size) biopsy punch to carefully center the craniotomy over the AAV injection site while avoiding the sagittal suture, and slowly and gently rotated the biopsy punch until the bone could be lifted away with 5/45 forceps. We used saline to irrigate regularly while performing the craniotomy, taking care not to puncture the dura. After stopping any bleeding, we placed a small amount of silicone oil (Sigma-Aldrich Inc. # 181838) to cover the brain, then carefully placed the stacked window over the brain. We then applied pressure to the top of the stacked window with a thinned wooden applicator (e.g. back of a cotton swab or toothpick) mounted on the stereotaxic arm until the 4 mm (or 5 mm) coverslip was flush with the skull surface. We used cyanoacrylate to glue around the window and waited until it dried before removing pressure from the thinned wooden applicator. We then positioned the headpost over the skull and used C&B Metabond to cement the headpost in place, taking care not to cover the cranial window. After the Metabond dried, we applied some silicone elastomer (World Precision Instruments, Kwik-Sil) over the cranial window to protect it from any damage. We then administered post-operative drugs (meloxicam at 5 mg/kg and 0.25% Bupivicaine around the headpost implant) and allowed the mouse to recover for at least 3 days before imaging.

Recording sessions

Prior to each animal's first awake head-fixed imaging session, the animals were acclimated to head-fixation and the treadmill set-up for at least three sessions. Additionally, to minimize stress prior to awake imaging session, we acclimated the animals to mechanical fixation in which the head was restrained. Animals received chocolate milk (Nesquik) as a reward while running on a custom-built treadmill. Once acclimated, animals were imaged for up to two sessions per day, where each session lasted no longer than two hours.

For experiments, mice were head-fixed atop a freely moving treadmill during video capture. Epifluorescence microscope images were captured with a sCMOS camera (Kiralux, 5 MP) through a 4× objective. Treadmill rotation data (synchronized with the camera) was captured during the experiment. During the recording session, a brushing tactile stimulus was applied to the spine region of the mouse with a minimum of 30 s between stimulus events. Bio-FlatScope recording sessions were captured within 30 minutes of epifluorescence recordings, with exposure time, recording lengths and stimuli timing matching those with the epifluorescence microscope. ROIs in the brain for comparing treadmill activity across epifluorescence and Bio-FlatScope were selected based on high activity areas extracted from the epifluorescence video.

RPCA analysis

This analysis was based on two-minute imaging sessions recorded at 20 Hz over the full FOV of the cranial window using both Bio-FlatScope and an epifluorescence microscope with a 4× objective. The ROIs for cluster analysis were selected by observing a 500 μm x 500 μm region of spontaneous high activity in the Bio-FlatScope reconstructions (Fig. 4a). This same ROI was used for both Bio-FlatScope and epifluorescence data. Figures 4b & c show the clusters extracted through k-means as well as the corresponding ΔF/F for those clusters.

Human subjects for oral mucosa imaging

The *in vivo* human study was performed at Rice University in Houston, TX. Volunteers recruited in the study were 18 years or older with no underlying health conditions. All volunteers provided health pre-screen information to reduce the risk of COVID spread. The study was in accord with the protocol approved by the Institutional Review Board at Rice University. Written informed consent was obtained from all volunteers prior to imaging.

In vivo oral mucosa imaging

464 Bio-FlatScope imaging and microscopic imaging were performed on each human volunteer. A
465 Bio-FlatScope prototype based on a contour phase mask with 6 μm feature size was used in
466 this experiment. During a Bio-FlatScope imaging session, volunteers were instructed to place
467 their chin and forehead on a custom chin-head rest for maximum stability (Fig. S13). The
468 illumination was achieved by a tabletop green LED (X-Cite XLED1) and a liquid light guide
469 (3 mm diameter) mounted in the chin rest with illumination intensity less than 20 mW. The
470 illumination source was used 3 to 5 minutes per imaging session, resulting in maximum
471 illumination intensity at skin less than the threshold limit value (TLV) specified by ACGIH.
472 During the experiment, the volunteer positioned his/her lower lip over the tip of the liquid light
473 guide with one hand and placed the imaging device onto the illuminated area with the other
474 hand. The imaging device consists of a Bio-FlatScope prototype and an opaque handheld
475 enclosure, designed to maintain a constant 3 mm working distance, with a 2.5 mm wide square
476 aperture.
477 The microscopic imaging session was performed with a microscope objective (Nikon Fluor
478 4×, NA 0.13 PhL DL). During the imaging session, the volunteer was instructed to position
479 his/her lower lip with one hand and hold the liquid light guide with the other hand to keep the
480 tip in contact with the bottom side of the lower lip.

481 *Human oral mucosa vessel counting*

482 Vessel counting was based on images taken by the 4× objective, and reconstructed images from
483 the Bio-FlatScope prototype. A grid containing 2 mm of horizontal lines and
484 2 mm of vertical lines was superimposed on the image. The capillary density was calculated
485 similar to the method in [46,47]. The number of small vessels (< 20 μm) per millimeter was
486 calculated as the number of small vessels crossing the grid divided by the total length of the
487 grid. Two researchers independently performed vessel counting for each image and the results
488 were averaged. In each volunteer, the images from ten different areas were averaged to give a
489 final capillary density value.

490

498 *Data and code*

499 The data and code that support the findings of this study are available from the authors upon
500 reasonable request.

501

502 **See Supplementary Information for supporting content**
503

References

1. J. Holloway, Y. Wu, M. K. Sharma, O. Cossairt, and A. Veeraraghavan, "SAVI: Synthetic apertures for long-range, subdiffraction-limited visible imaging using Fourier ptychography," Sci. Adv. **3**, e1602564 (2017).

2. Y. Wu, M. K. Sharma, and A. Veeraraghavan, "WISH: wavefront imaging sensor with high resolution," Light Sci. Appl. **8**, 44 (2019).

3. V. Boominathan, J. Adams, J. Robinson, and A. Veeraraghavan, "PhlatCam: Designed phase-mask based thin lensless camera," IEEE Trans. Pattern Anal. Mach. Intell. 1–1 (2020).

4. E. Betzig, G. H. Patterson, R. Sougrat, O. W. Lindwasser, S. Olenych, J. S. Bonifacino, M. W. Davidson, J. Lippincott-Schwartz, and H. F. Hess, "Imaging intracellular fluorescent proteins at nanometer resolution.," Science **313**, 1642–5 (2006).

5. M. J. Rust, M. Bates, and X. Zhuang, "Sub-diffraction-limit imaging by stochastic optical reconstruction microscopy (STORM)," Nat. Methods **3**, 793–796 (2006).

6. L. Tian and L. Waller, "3D intensity and phase imaging from light field measurements in an LED array microscope," Optica **2**, 104 (2015).

7. R. Prevedel, Y.-G. Yoon, M. Hoffmann, N. Pak, G. Wetzstein, S. Kato, T. Schrödel, R. Raskar, M. Zimmer, E. S. Boyden, and A. Vaziri, "Simultaneous whole-animal 3D imaging of neuronal activity using light-field microscopy," Nat Methods **11**, 727–730 (2014).

8. T. S. Ralston, D. L. Marks, P. Scott Carney, and S. A. Boppart, "Interferometric synthetic aperture microscopy," Nat Phys **3**, 129–134 (2007).

9. A. Ozcan and U. Demirci, "Ultra wide-field lens-free monitoring of cells on-chip.," Lab. Chip **8**, 98–106 (2008).

10. J. K. Adams, V. Boominathan, B. W. Avants, D. G. Vercosa, F. Ye, R. G. Baraniuk, J. T. Robinson, and A. Veeraraghavan, "Single-frame 3D fluorescence microscopy with ultraminiature lensless FlatScope," Sci. Adv. **3**, e1701548 (2017).

11. N. Antipa, G. Kuo, R. Heckel, B. Mildenhall, E. Bostan, R. Ng, and L. Waller, "DiffuserCam: lensless single-exposure 3D imaging," Optica **5**, 1 (2018).

12. A. Greenbaum, W. Luo, T.-W. Su, Z. Göröcs, L. Xue, S. O. Isikman, A. F. Coskun, O. Mudanyali, and A. Ozcan, "Imaging without lenses: achievements and remaining challenges of wide-field on-chip microscopy," Nat. Methods **9**, 889–895 (2012).

13. P. R. Gill and D. G. Stork, "Lensless Ultra-Miniature Imagers Using Odd-Symmetry Spiral Phase Gratings," Imaging Appl. Opt. CW4C.3 (2013).

14. S. Asif, A. Ayremlou, A. Sankaranarayanan, A. Veeraraghavan, and R. Baraniuk, "FlatCam: Thin, Lensless Cameras using Coded Aperture and Computation," IEEE Trans. Comput. Imaging 1 (2016).

15. V. Boominathan, J. K. Adams, M. S. Asif, B. W. Avants, J. T. Robinson, R. G. Baraniuk, A. C. Sankaranarayanan, and A. Veeraraghavan, "Lensless Imaging: A computational renaissance," IEEE Signal Process. Mag. **33**, 23–35 (2016).

16. R. Horisaki, Y. Ogura, M. Aino, and J. Tanida, "Single-shot phase imaging with a coded aperture," Opt Lett **39**, 6466–6469 (2014).

17. M. J. DeWeert and B. P. Farm, "Lensless coded aperture imaging with separable doubly Toeplitz masks," Opt. Eng. **54**, 023102 (2015).

18. G. Kuo, N. Antipa, R. Ng, and L. Waller, "DiffuserCam: Diffuser-Based Lensless Cameras," in *Imaging and Applied Optics 2017 (3D, AIO, COSI, IS, MATH, PcAOP)* (2017), p. CTu3B.2.

19. I. Sencan, A. F. Coskun, U. Sikora, and A. Ozcan, "Spectral demultiplexing in holographic and fluorescent on-chip microscopy.," Sci. Rep. **4**, 3760 (2014).

20. A. F. Coskun, I. Sencan, T.-W. Su, and A. Ozcan, "Lensless wide-field fluorescent imaging on a chip using compressive decoding of sparse objects.," Opt. Express **18**, 10510–23 (2010).

21. S. R. P. Pavani, M. A. Thompson, J. S. Biteen, S. J. Lord, N. Liu, R. J. Twieg, R. Piestun, and W. E. Moerner, "Three-dimensional, single-molecule fluorescence imaging beyond the diffraction limit by using a double-helix point spread function," Proc Natl Acad Sci U A **106**, 2995–2999 (2009).

22. J. Chen, M. Hirsch, R. Heintzmann, B. Eberhardt, and H. P. A. Lensch, "A Phase-coded Aperture Camera with Programmable Optics," Electron. Imaging **2017**, 70–75 (2017).

23. Y. Wu, V. Boominathan, H. Chen, and Others, "PhaseCam3D—Learning Phase Masks for Passive Single View Depth Estimation," 2019 IEEE (2019).

24. J. Chang, V. Sitzmann, X. Dun, W. Heidrich, and G. Wetzstein, "Hybrid optical-electronic convolutional neural networks with optimized diffractive optics for image classification," Sci Rep **8**, 12324 (2018).

25. W. Chi and N. George, "Optical imaging with phase-coded aperture," Opt Express **19**, 4294 (2011).

26. W. Wang, F. Ye, H. Shen, N. A. Moringo, C. Dutta, J. T. Robinson, and C. F. Landes, "Generalized method to design phase masks for 3D super-resolution microscopy," Opt Express **27**, 3799–3816 (2019).

27. K. N. Badhiwala, D. L. Gonzales, D. G. Vercosa, B. W. Avants, and J. T. Robinson, "Microfluidics for electrophysiology, imaging, and behavioral analysis of Hydra," Lab Chip **18**, 2523–2539 (2018).

28. C. Dupre and R. Yuste, "Non-overlapping Neural Networks in Hydra vulgaris," Curr Biol **27**, 1085–1097 (2017).

29. C. E. Juliano, H. Lin, and R. E. Steele, "Generation of transgenic Hydra by embryo microinjection.," J. Vis. Exp. JoVE 51888 (2014).

568 30. Badhiwala, K. N., Primack, A. S., Juliano, C. E. & Robinson, J. T. Multiple nerve rings coordinate Hydra
569   mechanosensory behavior. 1–28 (2020).
570 31. J. R. Szymanski and R. Yuste, "Mapping the whole-body muscle activity of Hydra vulgaris," Curr Biol (2019).
571 32. C. N. Tzouanas, S. Kim, K. N. Badhiwala, B. W. Avants, and J. T. Robinson, "Thermal stimulation temperature
572   is encoded as a firing rate in a Hydra nerve ring," bioRxiv 787648 (2019).
573 33. D. A. Dombeck, M. S. Graziano, and D. W. Tank, "Functional Clustering of Neurons in Motor Cortex
574   Determined by Cellular Resolution Imaging in Awake Behaving Mice," J. Neurosci. 29, 13751–13760 (2009).

575 34. R. Prevedel, A. J. Verhoef, A. J. Pern\'ıa-Andrade, S. Weisenburger, B. S. Huang, T. Nöbauer, A. Fernández,
576   J. E. Delcour, P. Golshani, A. Baltuska, and A. Vaziri, *Fast Volumetric Calcium Imaging across Multiple
577   Cortical Layers Using Sculpted Light*, No. 12 (2016), Vol. 13.
578 35. N. J. Sofroniew, D. Flickinger, J. King, and K. Svoboda, "A large field of view two-photon mesoscope with
579   subcellular resolution for in vivo imaging," Elife **5**, (2016).
580 36. D. A. Dombeck, A. N. Khabbaz, F. Collman, T. L. Adelman, and D. W. Tank, "Imaging large-scale neural
581   activity with cellular resolution in awake, mobile mice," Neuron **56**, 43–57 (2007).
582 37. R. Tomer, M. Lovett-Barron, I. Kauvar, A. Andalman, V. M. Burns, S. Sankaran, L. Grosenick, M. Broxton,
583   S. Yang, and K. Deisseroth, "SPED Light Sheet Microscopy: Fast Mapping of Biological System Structure and
584   Function," Cell **163**, 1796–1806 (2015)
585 38. K. K. Ghosh, L. D. Burns, E. D. Cocker, A. Nimmerjahn, Y. Ziv, A. E. Gamal, and M. J. Schnitzer,
586   "Miniaturized integration of a fluorescence microscope," Nat Methods **8**, 871–878 (2011).
587 39. M. P. Vanni, A. W. Chan, M. Balbi, G. Silasi, and T. H. Murphy, "Mesoscale Mapping of Mouse Cortex
588   Reveals Frequency-Dependent Cycling between Distinct Macroscale Functional Modules," J. Neurosci. 37,
589   7513–7533 (2017).
590 40. Rynes, M. et al. Miniaturized head-mounted device for whole cortex mesoscale imaging in freely behaving
591   mice. (2020). doi:10.1101/2020.05.25.114892
592 41. D. Barson, A. S. Hamodi, X. Shen, G. Lur, R. T. Constable, J. A. Cardin, M. C. Crair, and M. J. Higley,
593   "Simultaneous mesoscopic and two-photon imaging of neuronal activity in cortical circuits," Nat. Methods 17,
594   107–113 (2020).
595 42. E. A. Pnevmatikakis and A. Giovannucci, "NoRMCorre: An online algorithm for piecewise rigid motion
596   correction of calcium imaging data," J. Neurosci. Methods **291**, 83–94 (2017).
597 43. A. Samaniego, V. Boominathan, A. Sabharwal, and A. Veeraraghavan, "mobileVision," in *Proceedings of the
598   Wireless Health 2014 on National Institutes of Health - WH '14* (ACM Press, 2014), pp. 1–8.
599 44. E. J. Candes, X. Li, Y. Ma, and J. Wright, "Robust Principal Component Analysis?," J. ACM **58**, (2011).
600 45. Z. Lin, A. Ganesh, J. Wright, and L. Wu, "Fast convex optimization algorithms for exact recovery of a corrupted
601   low-rank matrix," Comput. Adv. Ldots 1–18 (2009).
602 46. Trzeciak, S. et al. Early microcirculatory perfusion derangements in patients with severe sepsis and septic
603   shock: Relationship to hemodynamics, oxygen transport, and survival. Annals of Emergency
604   Medicine **49**, (2007).
605 47. De Backer, D. et al. Microcirculatory alterations in patients with severe sepsis: Impact of time of assessment
606   and relationship with outcome. Critical Care Medicine **41**, 791–799 (2013).
607 48. Takano, J. H. et al. Detecting early oral cancer: narrowband imaging system observation of the oral mucosa
608   microvasculature. International Journal of Oral and Maxillofacial Surgery **39**, 208–213 (2010).
609 49. Yang, S. W. et al. Clinical characteristics of narrow-band imaging of oral erythroplakia and its correlation with
610   pathology. BMC Cancer **15**, (2015).
611 50. Bastos, P. & Cook, R. Real Time Optical Vascular Imaging: A Potential Technique for the Diagnosis of
612   Mucosal Disease Including Early Oral Cancer. Primary dental journal **5**, 86–91 (2016).
613 51. Ide, E., Maluf-Filho, F., Chaves, D. M., Matuguma, S. E. & Sakai, P. Narrow-band imaging without
614   magnifcation for detecting early esophageal squamous cell carcinoma. World Journal of
615   Gastroenterology **17**, 4408–4413 (2011).
616 52. Tan, N. C. W., Herd, M. K., Brennan, P. A. & Puxeddu, R. The role of narrow band imaging in early detection
617   of head and neck cancer. British Journal of Oral and Maxillofacial Surgery **50**, 132–136 (2012).
618 53. Ide, E. et al. Endoscopic detection of early esophageal squamous cell carcinoma in patients with achalasia:
619   Narrow-band imaging versus Lugol's staining. Journal of Oncology (2013). doi:10.1155/2013/736756
620 54. Sharma, P. et al. Development and Validation of a Classification System to Identify High-Grade Dysplasia and
621   Esophageal   Adenocarcinoma   in   Barrett's   Esophagus   Using   Narrow-Band
622   Imaging. Gastroenterology 150, 591–598 (2016).
623 55. Hanahan, D. & Weinberg, R. A. Hallmarks of cancer: The next generation. Cell **144**, 646–674 (2011).
624 56. Wang, J. Z. et al. Clinicopathological and prognostic significance of blood microvessel density in endometrial
625   cancer: a meta-analysis and subgroup analysis. Archives of Gynecology and Obstetrics **297**, 731–740 (2018).
626 57. Ma, G. et al. Microvessel density as a prognostic factor in esophageal squamous cell cancer patients. Medicine
627   (United States) **96**, (2017).
628 58. C. Richard, A. Renaudin, V. Aimez, and P. G. Charette, "An integrated hybrid interference and absorption filter
629   for fluorescence detection in lab-on-a-chip devices.," Lab. Chip **9**, 1371–1376 (2009).

59. M. B. Bouchard, V. Voleti, C. S. Mendes, C. Lacefield, W. B. Grueber, R. S. Mann, R. M. Bruno, and E. M. C. Hillman, "Swept confocally-aligned planar excitation (SCAPE) microscopy for high-speed volumetric imaging of behaving organisms," Nat. Photonics **9**, 113–119 (2015).

60. F. Ye, B. W. Avants, A. Veeraraghavan, and J. T. Robinson, "Integrated light-sheet illumination using metallic slit microlenses," Opt. Express **26**, 27326–27338 (2018).

61. D. Miyamoto and M. Murayama, "The fiber-optic imaging and manipulation of neural activity during animal behavior," Neurosci Res **103**, 1–9 (2016).

62. L. Ghanbari, R. E. Carter, M. L. Rynes, J. Dominguez, G. Chen, A. Naik, J. Hu, M. A. K. Sagar, L. Haltom, N. Mossazghi, M. M. Gray, S. L. West, K. W. Eliceiri, T. J. Ebner, and S. B. Kodandaramaiah, "Cortex-wide neural interfacing via transparent polymer skulls," Nat Commun **10**, 1500 (2019).

63. G. J. Goldey, D. K. Roumis, L. L. Glickfeld, A. M. Kerlin, R. C. Reid, V. Bonin, D. P. Schafer, and M. L. Andermann, "Removable cranial windows for long-term imaging in awake mice," Nat Protoc **9**, 2515–2538 (2014).

In vivo imaging with a flat, lensless microscope: supplemental document

643
644
645
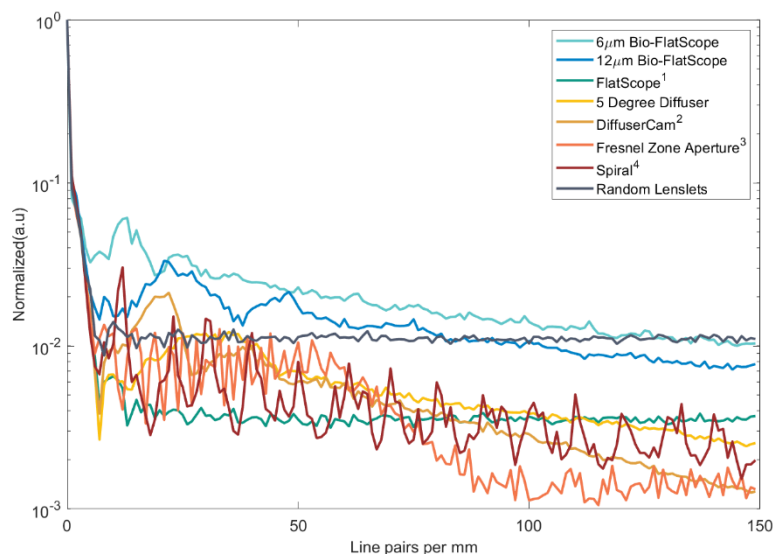
Fig. S1. Modulation transfer function (MTF) comparison among PSF designs used by lensless imaging systems.

646
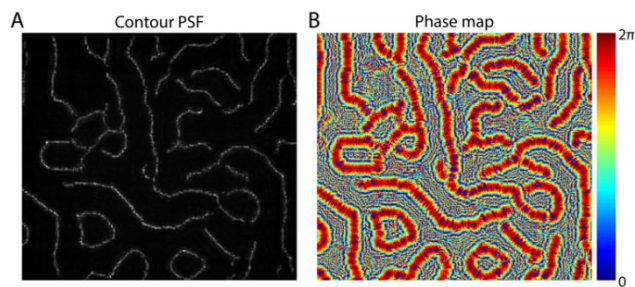
Fig. S2. (A) Contour-based PSF design provides robustness to noise and capturing many directional filters. (B) Phase map for the mask in order to produce the PSF on the image sensor.
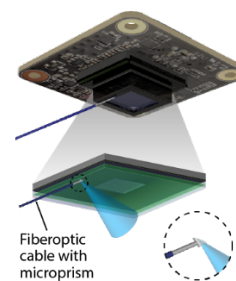

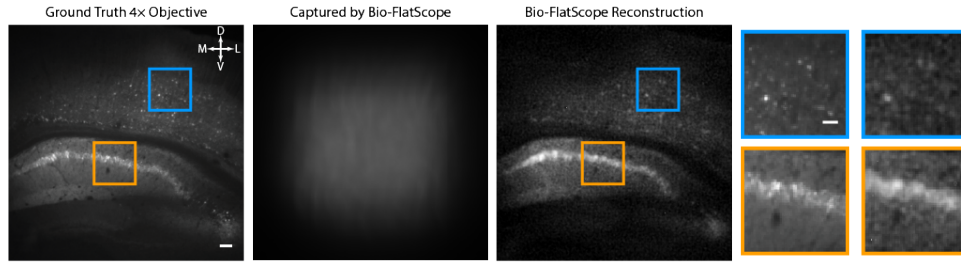**Fig. S3.** Bio-FlatScope with near-epi illumination with microprism and fiber-optic cable.

Fig. S4. Mouse brain slice imaging. Ground truth capture, raw capture by Bio-FlatScope, and Bio-FlatScope reconstruction of a mouse brain slice expressing GCaMP6f. The compass shows dorsal-D, ventral-D, medial-M and later-L directions. Scale bar, 100 μm. Far right shows zoom-in comparisons of ground truth and Bio-FlatScope reconstructions, respectively. Scale bar, 50 μm.
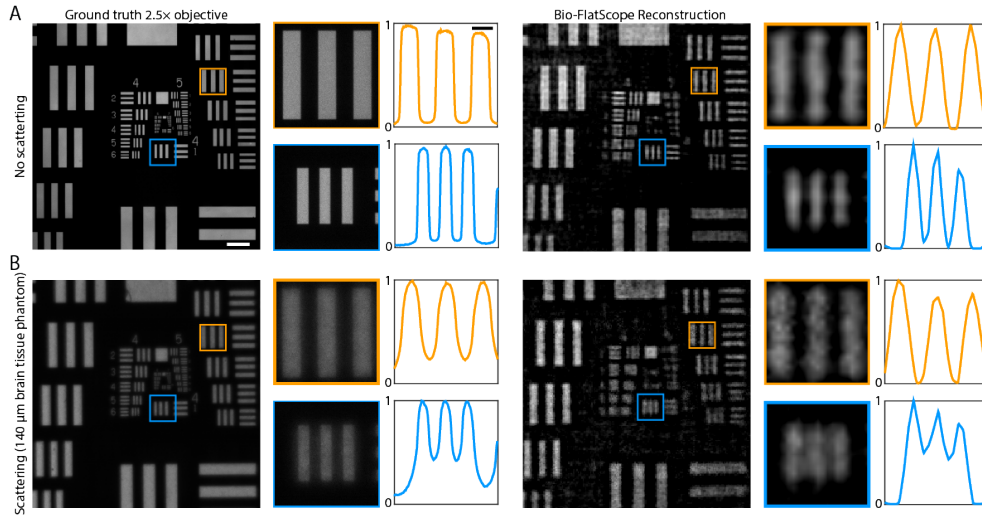
Fig. S5. Imaging through scattering medium. (A) Ground truth (left, captured with a 2.5× objective and Bio-FlatScope reconstruction (right, captured at ~8.5 mm from the device) of USAF 1951 resolution target. Scale bar, 250 μm. Zoom-ins are shown for Group 3 element 3 and group 4 element 1. Scale bar, 50 μm. (B) Ground truth (left, captured with a 2.5× objective) and Bio-FlatScope reconstruction (right, captured at ~8.5 mm from the device) of USAF 1951 resolution target captured through 140 μm of brain tissue phantom. Scale bar, 250 μm. Zoom-ins are shown for Group 3 element 3 and group 4 element 1. Scale bar, 50 μm.
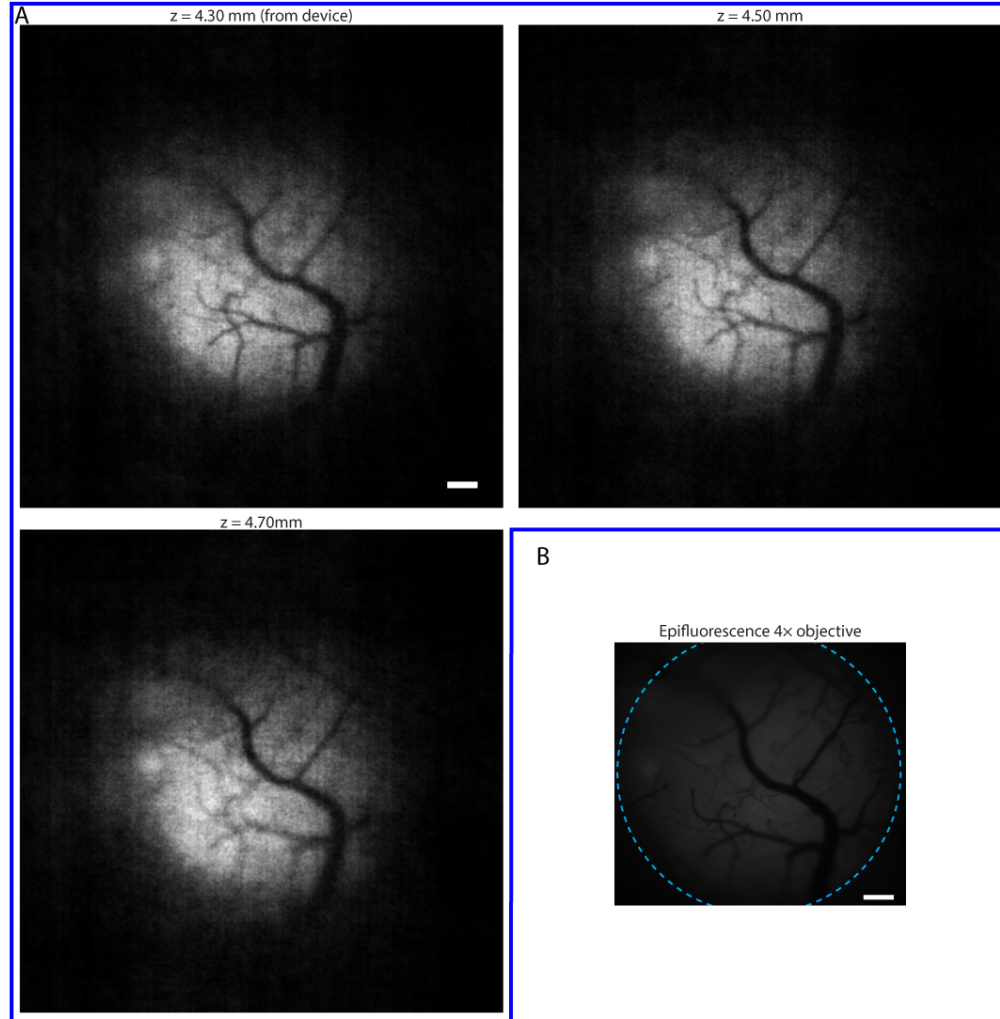
Fig. S6. Full Bio-FlatScope field of view for *in vivo* mouse brain recordings. (A) Full FOV Bio-FlatScope reconstructions of mouse brain *in vivo* at 4.3 mm, 4.5 mm, and 4.7 mm from the device. Dark areas (around edges) are regions located outside of the cranial window. Scale bar, 250 μm (B) Epifluorescence image of same region of the mouse brain captured with a 4× microscope objective. Dashed cyan line indicates the outer edge of the cranial window. Scale bar, 250 μm.
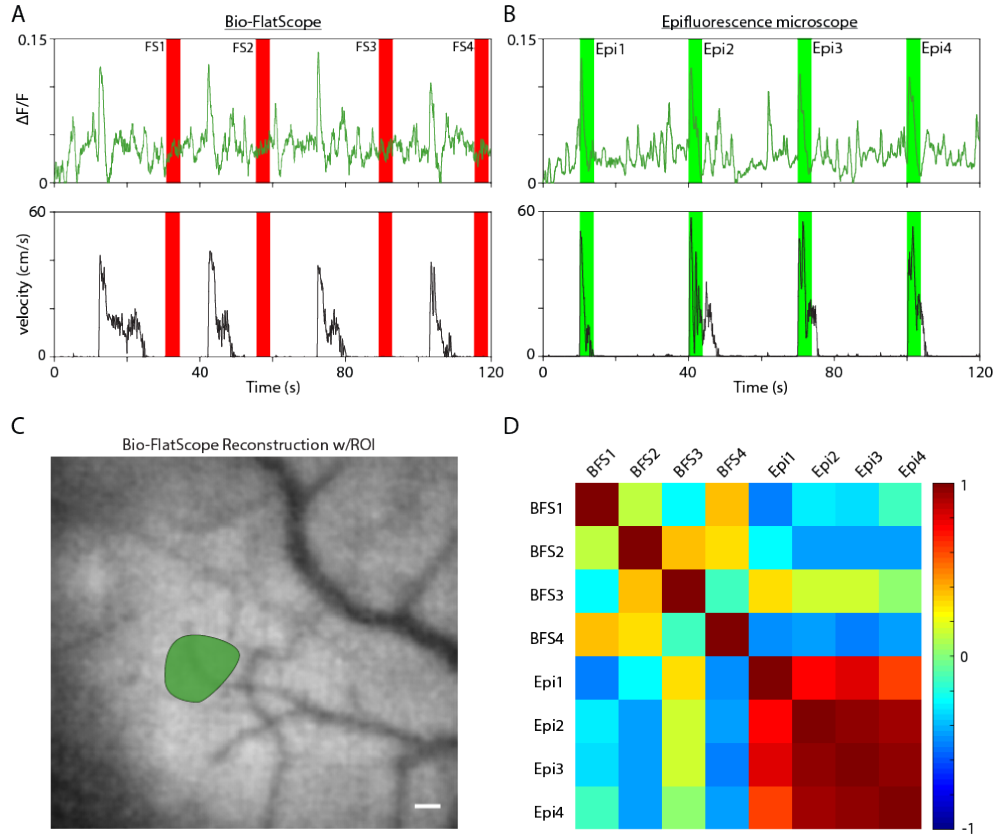
Fig. S7. Comparison of Bio-FlatScope Ca^{2+} responses during stationary periods to stimulus-evoked responses in epifluorescence recordings. (A) ΔF/F trace and treadmill velocity for Bio-FlatScope during recording session. The 4-second windows are selected when the mouse is stationary (having a velocity < 1 cm/s), shown in red. (B) ΔF/F trace and treadmill velocity for epifluorescence during recording session. The rising edge of the 4-second windows in green correspond to the application of tactile stimuli. (C) Bio-FlatScope reconstruction with a single ROI of high-activity marked. Scale bar, 100 μm. (D) Correlation matrix comparing the 4-second windows of little to no movement (red) and stimulus response activity (green). (BFS - Bio-FlatScope, Epi-Epifluorescence microscope).
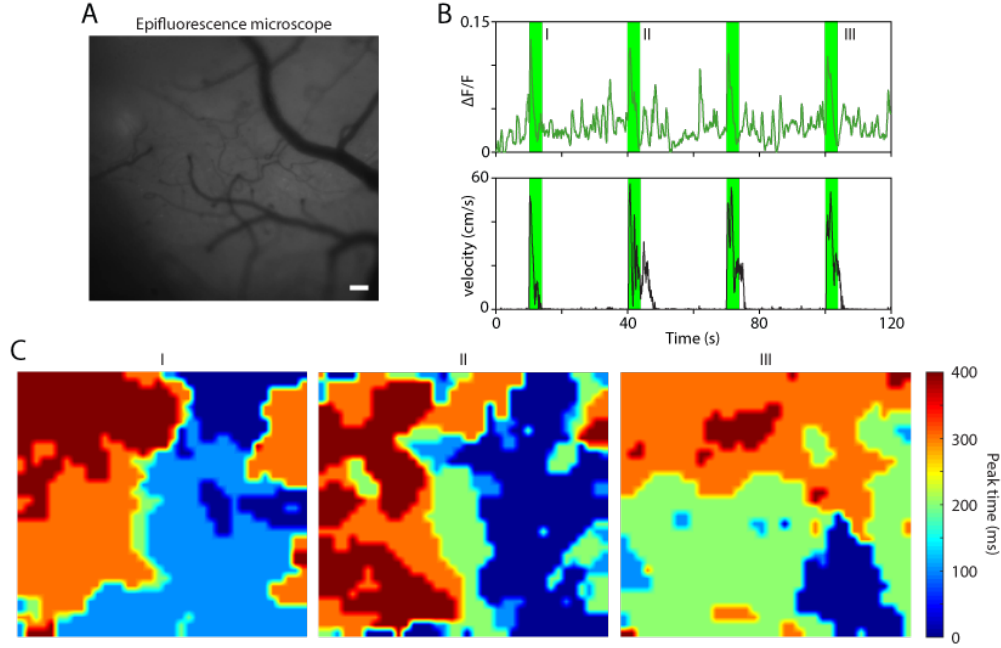
Fig. S8. Spatiotemporal Ca^{2+} dynamics from epifluorescence recording. (A) Single frame from epifluorescence microscope capture of ROI. Scale bar, 100 μm. (B) ΔF/F trace and treadmill velocity for epifluorescence during recording session. The rising edge of the 4-second windows in green correspond to the application of tactile stimuli. (C) Heat maps for epifluorescence captures showing spatiotemporal Ca^{2+} dynamics time-aligned with stimuli (at I, II, and III). Colormap shows the time at which pixels have their peak response for ΔF/F during a 400 ms period.
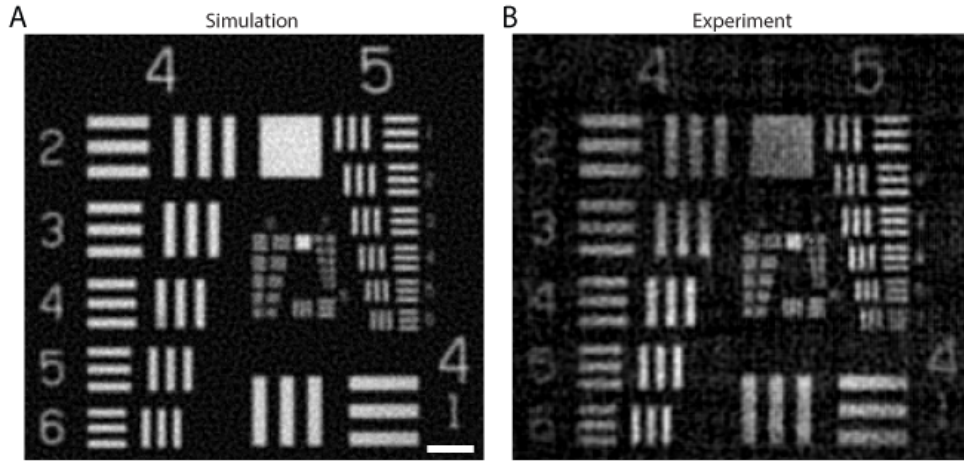

Fig. S9. Simulation vs experimental result of USAF. (A) Simulated Bio-FlatScope reconstruction of USAF target at 4.15 mm from device. Scale bar, 100 μm. (B) Experimental Bio-FlatScope reconstruction of USAF target at the same distance from device. The simulation result shows a very close match to the experimental result with group 5 element 6 being resolved.
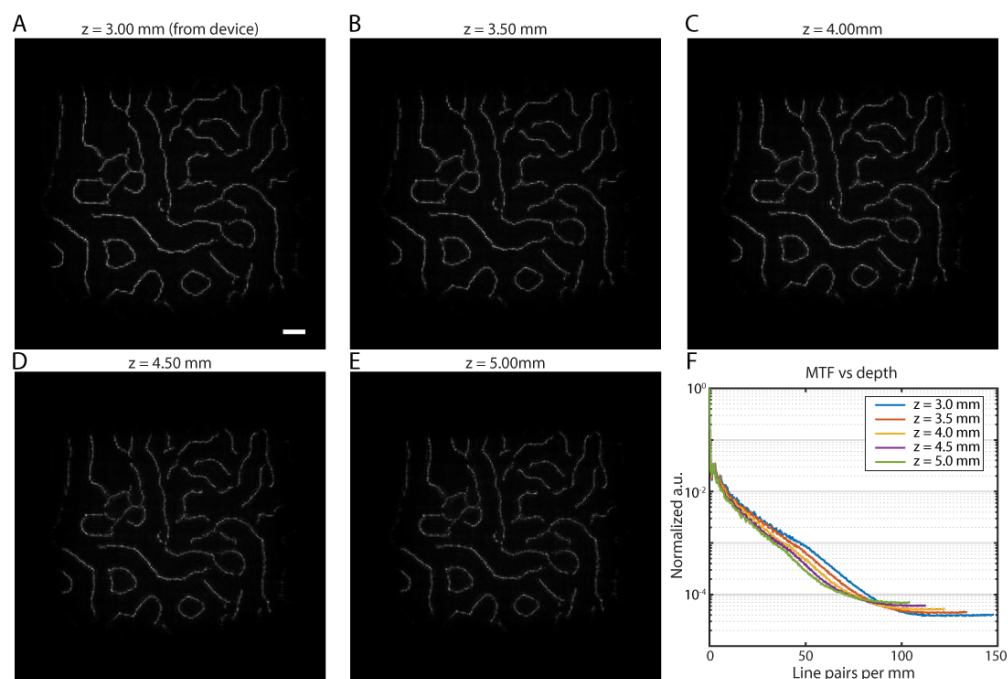
Fig. S10. Captured Bio-FlatScope point spread functions. Bio-FlatScope PSFs captured by imaging a 10 μm fluorescent microsphere (see *Methods*) at different depth planes of (A) 3.00 mm, (B) 3.50 mm, (C) 4.00 mm, (D) 4.50 mm, and (E) 5.00 mm. Scale bar, 100 μm. (F) Computed MTF from PSFs at different depths from Bio-FlatScope. We observe that the resolution decreases with increasing depth, as seen from the shifting of MTF curves to the left.
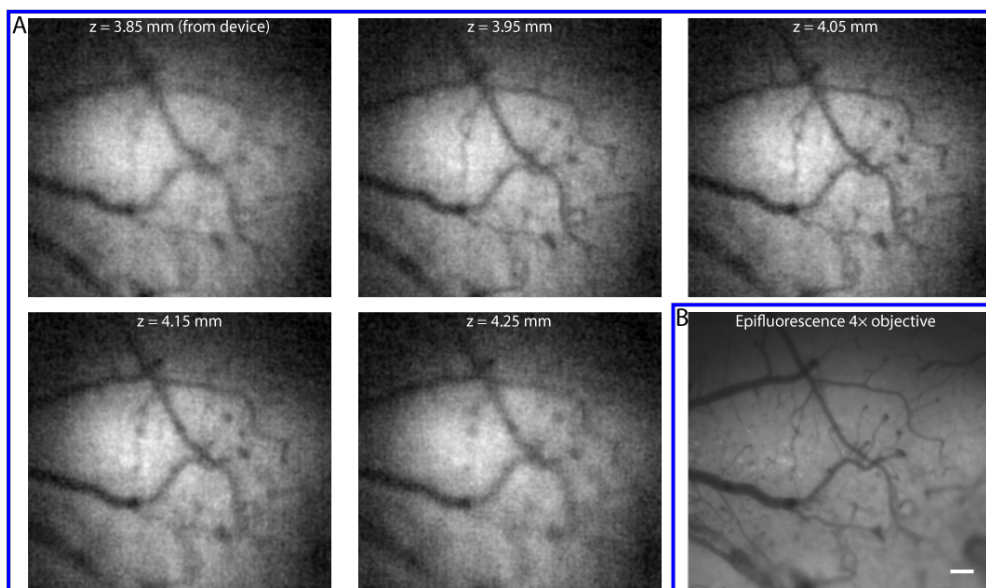

Fig. S11. Digitally refocusing in mouse brain. (A) Bio-FlatScope reconstructions for five different depth planes. At 4.05 mm, the image becomes sharpest for the FOV. (B) Epifluorescence image for the same FOV. Scale bar, 100 μm.
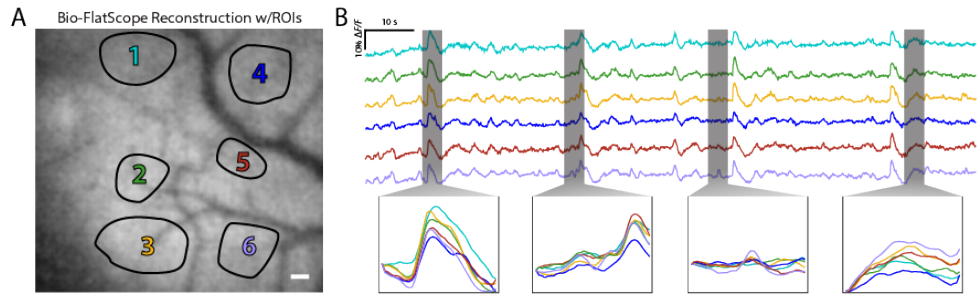
5

Fig. S12. Ca^{2+} responses from Bio-FlatScope recording across multiple ROIs. (A) Bio-FlatScope reconstruction showing multiple ROIs. Scale bar 100 μm. (B) ΔF/F traces for the multiple regions with zoom-ins showing differences in activity across ROIs.

Fig. S13. Oral mucosa imaging setup, including a chin-head rest and a liquid light guide connected to a tabletop LED source for illumination. This photo shows how the liquid light guide is mounted in the chin rest.

Table S1. Comparison of Bio-FlatScope to miniaturized, head-mounted microscopes.

Microscope[a]	Lateral resolution	Field of view
Bio-FlatScope	~8.8 µm	~16.2 mm^2
Integrated miniature microscope [5]	~2.5 µm	0.48 mm^2
Fiber bundle microscope [6]	~4.9 µm	~0.3 mm^2
Two-photon miniaturized microscope [7]	0.64 µm	~0.03 mm^2
Miniaturized light-field microscope [8]	6 µm	~0.42 mm^2

[a]Selected microscopes have cellular resolution capability and remain light enough (< 3 g) to be mounted on a mouse and allow free behavior without any support.

References

1. J. K. Adams, V. Boominathan, B. W. Avants, D. G. Vercosa, F. Ye, R. G. Baraniuk, J. T. Robinson, and A. Veeraraghavan, "Single-frame 3D fluorescence microscopy with ultraminiature lensless FlatScope," Sci. Adv. **3**, e1701548 (2017).
2. N. Antipa, G. Kuo, R. Heckel, B. Mildenhall, E. Bostan, R. Ng, and L. Waller, "DiffuserCam: lensless single-exposure 3D imaging," Optica 5, 1 (2018).
3. Tajima, K., Shimano, T., Nakamura, Y., Sao, M. & Hoshizawa, T. Lensless light-field imaging with multi-phased fresnel zone aperture. in 2017 IEEE International Conference on Computational Photography, ICCP 2017 - Proceedings (Institute of Electrical and Electronics Engineers Inc., 2017). doi:10.1109/ICCPHOT.2017.7951485
4. Stork, D. G. & Gill, P. R. Optical, Mathematical, and Computational Foundations of Lensless Ultra-Miniature Diffractive Imagers and Sensors. International Journal on Advances in Systems and Measurements 7, 201–208 (2014).
5. K. K. Ghosh, L. D. Burns, E. D. Cocker, A. Nimmerjahn, Y. Ziv, A. E. Gamal, and M. J. Schnitzer, "Miniaturized integration of a fluorescence microscope," Nat Methods 8, 871–878 (2011).
6. M. Kim, J. Hong, J. Kim, and H. Shin, "Fiber bundle-based integrated platform for wide-field fluorescence imaging and patterned optical stimulation for modulation of vasoconstriction in the deep brain of a living animal," Biomed. Opt. Express **8**, 2781 (2017).
7. W. Zong, R. Wu, M. Li, Y. Hu, Y. Li, J. Li, H. Rong, H. Wu, Y. Xu, Y. Lu, H. Jia, M. Fan, Z. Zhou, Y. Zhang, A. Wang, L. Chen, and H. Cheng, "Fast high-resolution miniature two-photon microscopy for brain imaging in freely behaving mice," Nat Methods 14, 713–719 (2017).
8. O. Skocek, T. Nöbauer, L. Weilguny, F. Mart\'ınez Traub, C. N. Xia, M. I. Molodtsov, A. Grama, M. Yamagata, D. Aharoni, D. D. Cox, P. Golshani, and A. Vaziri, "High-speed volumetric imaging of neuronal activity in freely moving rodents," Nat. Methods **15**, 1–4 (2018).